

Phase error compensation for three-dimensional shape measurement with projector defocusing

Ying Xu,¹ Laura Ekstrand,¹ Junfei Dai,² and Song Zhang^{1,*}

¹Department of Mechanical Engineering, Iowa State University, Ames, Iowa 50011, USA

²Department of Mathematics, Zhejiang University, Hangzhou, Zhejiang 310029, China

*Corresponding author: song@iastate.edu

Received 13 October 2010; revised 9 February 2011; accepted 4 April 2011;
posted 5 April 2011 (Doc. ID 136516); published 2 June 2011

This paper analyzes the phase error for a three-dimensional (3D) shape measurement system that utilizes our recently proposed projector defocusing technique. This technique generates seemingly sinusoidal structured patterns by defocusing binary structured patterns and then uses these patterns to perform 3D shape measurement by fringe analysis. However, significant errors may still exist if an object is within a certain depth range, where the defocused fringe patterns retain binary structure. In this research, we experimentally studied a large depth range of defocused fringe patterns, from near-binary to near-sinusoidal, and analyzed the associated phase errors. We established a mathematical phase error function in terms of the wrapped phase and the depth z . Finally, we calibrated and used the mathematical function to compensate for the phase error at arbitrary depth ranges within the calibration volume. Experimental results will be presented to demonstrate the success of this proposed technique. © 2011 Optical Society of America

OCIS codes: 120.0120, 120.2650, 120.5050.

1. Introduction

Three-dimensional (3D) shape measurement based on a digital fringe projection technique, which has recently become mainstream, has numerous advantages in comparison with other structured light techniques including its measurement speed and accuracy [1]. Because of its simplicity and high spatial resolution, this technique has had some success for high-resolution, real-time applications [2].

A conventional digital fringe projection system usually uses a commercially available digital-light-processing (DLP) projector to project computer-generated sinusoidal fringe patterns. This technique can achieve reasonable speed and accuracy. However, for high-speed and high-accuracy 3D measurement, there are three major issues to consider: (1) the nonlinearity of the projection system, (2) the requirement of precise synchronization between the camera

and the projector, and (3) the speed bottleneck of the projector (120 Hz) [3].

To alleviate the aforementioned problems associated with a conventional fringe projection system, we recently proposed a new technique for 3D shape measurement that utilizes the natural phenomenon of projector defocusing [4]. In this technique, instead of sending sinusoidal fringe patterns to the projector, only binary structured patterns are used. The sinusoidal fringe patterns are generated by properly defocusing the projector. For this technique, because only two grayscale values (0's and 255's) are used, the nonlinear projection of the projector will not affect the measurement accuracy. In principle, the DLP projector generates grayscale values by time modulation [5]. That is, the micromirror flips on and off rapidly so that the percentage of on time represents the percentage of the full grayscale value (255). This means that (1) to generate a grayscale value of 0, the micromirror is always at an off status (0% on); (2) to generate a grayscale value of 255, the micromirror is always at an on status (100% on); and (3) to generate

a grayscale value of 128, the micromirror is at an on status about half the time (50% on). Therefore, if only 0 and 255 grayscale values are used, each micromirror will remain stationary. In other words, it will not flip on/off for the projection time of each particular channel. This indicates that any period of time can represent the input signal, and thus the camera does not need to be precisely synchronized with the projector to correctly capture the structured patterns.

By taking advantage of the unique features of this defocusing technology, we have successfully improved our real-time 3D shape measurement system speed to 120 Hz [6]. Moreover, because the fringe pattern is a “solid state,” Gong and Zhang [7] have demonstrated that the 3D shape measurement speed can be as fast as tens of kilohertz using an off-the-shelf inexpensive DLP projector (Dell M109S) with the Fourier fringe analysis method [8]. Therefore, the speed bottleneck of using a commercially available DLP projector does not exist if the defocusing technique is adopted. In addition, with advanced hardware, such as the DLP Discovery platform developed by Texas Instruments, ultrafast phase shifting can be achieved, and unprecedentedly high-speed 3D shape measurement becomes feasible. Specifically, we have developed a method by which we could reach 667 Hz 3D shape measurement by utilizing a three-step phase-shifting approach with the DLP Discovery D4000 projection platform [9].

However, the projector-defocusing-based technology is not trouble free. Figure 1 illustrates a projector’s natural behavior of defocusing with increasing depth, z . At the focal plane, a projected binary structured pattern has no distortion. In region A, the pattern begins to defocus but retains significant binary structure. In the narrow region B, the pattern develops into high-quality sinusoidal fringe patterns. In region C, the signal becomes too weak relative to the noise for use in 3D shape measurement. We found that there are significant phase errors if an object is not within region B. Therefore, compared to a conventional fringe projection technique where the

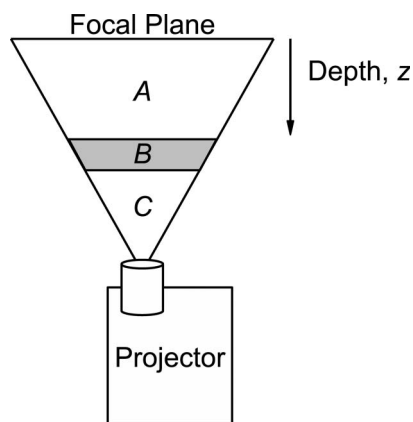


Fig. 1. Projector defocusing with increasing depth. While region B develops high-quality sinusoidal fringe patterns, the patterns of region A retain binary structure, which results in phase errors. The signal-to-noise ratio of region C renders it unusable.

fringe patterns retain their sinusoidal structure throughout the whole range, the depth range of this defocusing technique is much smaller. To increase the depth range, the phase error needs to be dramatically reduced in region A. One approach is to establish a relationship between phase error and depth. Then a compensation method can be adopted for the phase error if the depth is known.

Defocusing technology has been used to remove pixel effects for a long time. But in our research we used this technique to generate sinusoidal fringe patterns for 3D shape measurement. It should be noted that Su *et al.* has used the defocusing technology for 3D shape measurement with a Ronchi grating [10]. Because the Ronchi grating is a mechanical device, it is not easy to change fringe pitches or to shift the phase. A digital fringe projection technique, on the other hand, precisely controls the phase shift and adjusts the fringe pitch easily. Therefore, it is advantageous to use such a technology for 3D shape measurement. Unlike a grating-based technique where the phase error caused by phase shift may be dominant, the digital fringe projection technique does not have this type of error due to its digital fringe generation nature. Therefore, the phase errors caused by other sources need to be considered and reduced for high-quality measurement.

In this research, we experimentally studied a large depth range of defocused fringe patterns, from near-binary to near-sinusoidal, and analyzed the associated phase errors. We established a mathematical phase error function in terms of the wrapped phase and the depth z . Finally, we calibrated and used the mathematical function to compensate for the phase error at arbitrary depth ranges within the calibration volume. To quantify the phase error, a uniform, flat white board is placed in front of the system and moved closer to or further away from the system. For each position, the phase error is analyzed and stored in a lookup table (LUT). We found that these LUTs can be approximated as a high-order polynomial function for each plane; this is called the intraplane polynomial fitting. Moreover, we found that at different depths, the phase error has the same structure in terms of wrapped phase but different amplitude. Therefore, the amplitude can then be approximated as another set of polynomial functions in terms of depth, z ; this is called the interplane polynomial fitting. This method of fitting polynomials to both the intraplane and interplane data is called dual-stage polynomial (DSP) fitting. Because the intraplane phase error requires a high-order polynomial fitting, a method is also proposed that uses a direct LUT for the intraplane representation and a low-order polynomial fitting for the interplane representation. This method is called polynomial LUT (PLUT), since each element of the LUT is a polynomial function in terms of z . Once the phase error function is calibrated, the phase error can be compensated for a given wrapped phase value and depth z . Experiments can then be

performed to verify the effectiveness of this proposed phase error compensation technique.

Section 2 briefly explains the principles of the defocusing technology and the three-step phase-shifting algorithm. Section 3 analyzes the phase errors and presents the error compensation methodology. Section 4 shows some preliminary experimental results that demonstrate the success of the proposed error compensation technique. Finally, Section 5 summarizes this paper.

2. Principles

A. Fundamentals of Defocusing Technology

Our recent study showed that by properly defocusing a binary structured pattern, a quasi-sinusoidal fringe pattern can be generated, and by spatially moving the binary structured pattern, a phase shift can be introduced. Therefore, this technique can achieve 3D shape measurement based on digital fringe projection and phase shifting [4]. To illustrate the viability of generating sinusoidal fringe patterns by defocusing binary structured ones, we conducted an experiment. In this simple experiment, we used a Dell LED projector (Model: M109S) and a The Imaging Source digital USB CCD camera (Model: DMK 21BU04) to project and capture the images, respectively. The projector shines a computer-generated binary structured pattern onto a uniform, flat white surface, and the camera images the scattered structured pattern into a computer. During the experiment, the camera is always in focus, the target plane holds its position, and the projector's focal length is successively increased by adjusting its focal knob. This creates a situation similar to moving the surface along the depth (z) axis shown in Fig. 1.

Figure 2, as well as the associated Media 1, show some typical fringe patterns captured by the camera during this process. They clearly show that if the projector is defocused to different degrees, the binary structured pattern is distorted to different levels. Figure 2(a) shows the resulting binary structures when both the projector and the camera are in focus. Figures 2(a)–2(e) show that when the degree of defocusing increases, the binary structures become less and less clear, and the sinusoidal ones become more and more obvious. However, when the projector is defocused too much, the sinusoidal structures start diminishing, as indicated in Fig. 2(e) (this results in region C in Fig. 1). Figures 2(f)–2(j) plot the cross sections of the associated fringe patterns above. This experiment indicates that a seemingly sinusoidal fringe pattern can indeed be generated by properly defocusing a binary structured one.

B. Three-Step Phase-Shifting Algorithm

Phase-shifting methods have been extensively used in optical metrology because of their speed and accuracy [11]. Over the years, many phase-shifting algorithms have been developed, including three-step, four-step, double-step, etc. Differing in the number of fringe patterns used, they share the same characteristics of (1) performing measurement point by point, (2) automatically alleviating the influence of ambient light, (3) obtaining phase values ranging from $-\pi$ to $+\pi$, and (4) achieving better accuracy by using more fringe patterns. Among these algorithms, a three-step phase-shifting algorithm is usually adopted for high-speed applications because it requires the least number of fringe patterns to recover one 3D shape. Three fringe images with a phase shift of $2\pi/3$ can be represented as

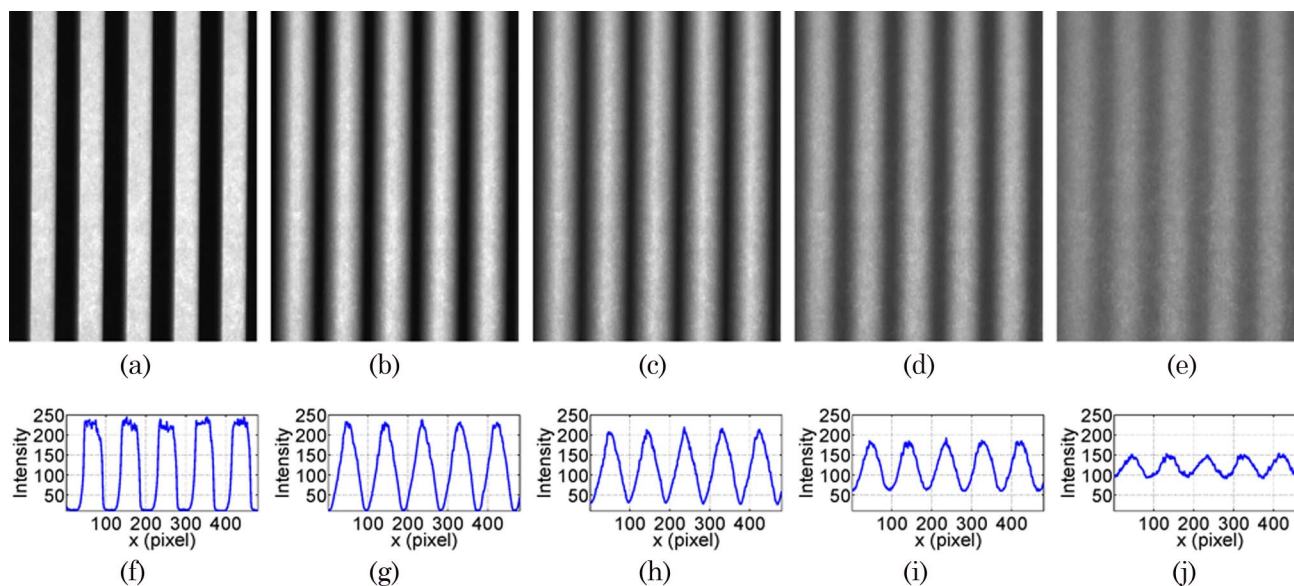


Fig. 2. (Color online) Example of sinusoidal fringe generation by defocusing binary structured patterns (Media 1). (a) Result when the projector is in focus. (b)–(e) The gradual results when the projector's focal length increases. (f)–(j) Illustrate the 240th row cross sections of the corresponding above fringe images.

$$I_1(x, y) = I'(x, y) + I''(x, y) \cos[\phi(x, y) - 2\pi/3], \quad (1)$$

$$I_2(x, y) = I'(x, y) + I''(x, y) \cos[\phi(x, y)], \quad (2)$$

$$I_3(x, y) = I'(x, y) + I''(x, y) \cos[\phi(x, y) + 2\pi/3]. \quad (3)$$

Here, $I'(x, y)$ is the average intensity, $I''(x, y)$ is the intensity modulation, and $\phi(x, y)$ is the phase. Simultaneously solving Eqs. (1)–(3) will give the phase

$$\phi(x, y) = \tan^{-1} \left[\sqrt{3}(I_1 - I_3)/(2I_2 - I_1 - I_3) \right]. \quad (4)$$

This equation only provides the phase value with a range of $[-\pi, +\pi)$. This is called the wrapped phase, and it can be unwrapped to obtain a continuous phase map, $\Phi(x, y)$, by adopting a phase-unwrapping algorithm [12]. A phase-unwrapping algorithm essentially locates the 2π discontinuous places in the wrapped map and removes them by adding or subtracting multiples of 2π . In other words, the phase unwrapping determines the integer number $m(x, y)$ for each point, so that

$$\Phi(x, y) = 2\pi \times m(x, y) + \phi(x, y). \quad (5)$$

However, this approach only works well for smaller depth ranges where the object movement does not cause phase changes of more than π . Moreover, because the unwrapped phase is relative to one point, the phase value obtained in Eq. (5) is typically the relative phase, which is difficult to uniquely correlate with the depth z value. To uniquely determine the relationship between depth z and the phase value, absolute phase is needed, which will be addressed next.

C. Absolute Phase Recovery I: Multiple Wavelength Technique

To obtain the absolute phase value, a multiple-wavelength phase-shifting technique can be adopted. In this research, we adopted the multiple-wavelength phase-shifting technique introduced in [13]. Specifically, assume the projector has a resolution of $W \times H$, and the projected fringe images are vertical. If we choose wavelength $\lambda_1 = W$, the unwrapping step is not required because the single fringe covers the whole measurement area. That is,

$$\Phi_1(x, y) = \phi_1(x, y). \quad (6)$$

Here $\Phi_1(x, y)$ represents the unwrapped phase, and $\phi_1(x, y)$ the wrapped phase.

For the phase $\phi_2(x, y)$ obtained from wavelength $\lambda_2 = \lambda_1/2$, there will be two fringes in the measurement area. Hence,

$$\Phi_2(x, y) = 2\pi m_2(x, y) + \phi_2(x, y). \quad (7)$$

Here $m_2(x, y)$ is an integer. Because $\lambda_1 = 2\lambda_2$, we have

$$\Phi_2 = 2\Phi_1. \quad (8)$$

That is,

$$m_2(x, y) = \text{Round} \left[\frac{\Phi_1(x, y)}{\pi} - \frac{\phi_2(x, y)}{2\pi} \right]. \quad (9)$$

Here, the Round[] operator is employed to obtain the closest integer value. Therefore, the wrapped phase, $\phi_2(x, y)$, can be unwrapped pixel by pixel by referring to the unwrapped longer wavelength phase $\Phi_1(x, y)$.

Once $\Phi_2(x, y)$ is obtained, we can use it to correct $\Phi_3(x, y)$, where $\lambda_3 = \lambda_2/2$, using an equation similar to Eq. (9). In general, for $\lambda_k = \lambda_{k-1}/2$,

$$m_k(x, y) = \text{Round} \left[\frac{\Phi_{k-1}(x, y)}{\pi} - \frac{\phi_k(x, y)}{2\pi} \right], \quad (10)$$

$$\Phi_k(x, y) = 2\pi m_k(x, y) + \phi_k(x, y). \quad (11)$$

Equation (10) shows that the unwrapped phase is obtained pixel by pixel without spatial phase unwrapping. Therefore, the phase is called absolute phase, because the phase on the camera is uniquely corresponding to the phase on the projector.

D. Absolute Phase Recovery II: Introduction of Gray Code

The aforementioned multiple-wavelength phase-shifting technique can be used to determine absolute phase point by point with high precision. However, it requires all fringe patterns to be sinusoidal. For the binary defocusing technique, it is difficult to realize sinusoidal fringe patterns with different wavelengths at the same depth; wider wavelengths do not defocus as much as narrower wavelengths at the same depth. Equation (11) indicates that as long as integer number $m(x, y)$ can be determined, the phase can be unwrapped, and if $m(x, y)$ can be uniquely determined, the unwrapped phase will be absolute. This leads to a technique that uses gray code to determine $m(x, y)$ through the use of binary structured patterns. In this research, we use the framework described in [14] for absolute phase determination.

In brief, a unique codeword $m(x, y)$, is assigned to each 2π phase-change period and is used to unwrap the phase obtained from phase-shifted fringe images. Each codeword consists of a sequence of binary structured patterns, and the codewords change from period to period according to the rules of gray code. The codeword patterns are wider than the phase-shifting fringe patterns; during projection, the narrowest binary patterns become sinusoidal fringe patterns, while the wider binary patterns are only slightly deformed. During image processing, the wider, deformed patterns are binarized to retrieve the

codewords. Finally, the codewords are used to unwrap the phase point by point.

E. Absolute-Phase-to-Depth Conversion

Once the absolute phase value is obtained for each camera pixel, the depth z value can be determined. In this paper, we utilize a reference-plane-based technique similar to the one introduced in [9] to convert absolute phase to depth z . Figure 3 shows the schematic diagram of the system.

Points P and I are the center of the exit pupil of the DLP projector and that of the CCD camera, respectively. After the system has been set up, a flat reference plane is measured first whose phase map is used as the reference for subsequent measurements. The height of the object surface is measured relative to this plane. From the point of view of the projector, point D on the object surface has the same phase value as point C on the reference plane, $\Phi_D = \Phi_C$. On the camera sensor, point D on the object surface and point A on the reference plane are imaged on the same pixel, $\Phi_A \leftarrow \Phi_D$. By subtracting the reference phase map from the object phase map, we obtained the phase difference at this specific pixel:

$$\Delta\Phi_{DA} = \Phi_D - \Phi_A = \Phi_C - \Phi_A = \Delta\Phi_{AC} \quad (12)$$

Assume points P and I are designed to be on the same plane with a distance l to the reference plane and have a fixed distance d between them. Assume also that the reference plane is parallel to the plane of the projector lens. Thus, $\triangle PID$ and $\triangle CAD$ are similar, and the height \overline{DB} of point D on the object surface relative to the reference plane can be related to the distance between points A and C ,

$$\Delta z(x,y) = \overline{DB} = \frac{\overline{AC} \cdot l}{d + \overline{AC}} \approx \frac{l}{d} \overline{AC} \propto \Delta\Phi_{AC} = \Phi_D - \Phi_A, \quad (13)$$

assuming d is much larger than \overline{AC} for real measurement. Combining Eqs. (12) and (13), a proportional relationship between the phase map and the surface

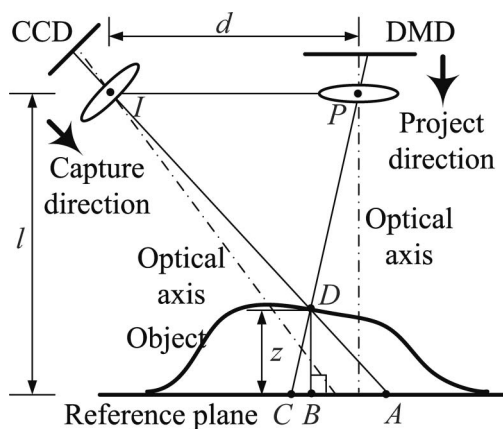


Fig. 3. Schematic diagram of phase-to-height conversion.

relative height can be derived point by point. That is, in general,

$$\Delta z \propto \Delta\Phi(x,y) = \Phi(x,y) - \Phi^r(x,y). \quad (14)$$

Here, $\Phi(x,y)$ is the object phase map, and $\Phi^r(x,y)$ is the reference phase map. Assuming the reference plane has a depth of z_0 , the absolute depth value for each measured point can be represented as

$$z(x,y) = z_0 + c_0 \times [\Phi(x,y) - \Phi^r(x,y)], \quad (15)$$

where c_0 is a constant that can be determined through calibration.

3. Phase Error Analysis

A. Experimental System Setup

Figure 4 shows a photograph of the experimental system setup. The 3D shape measurement system includes a DLP projector (Model: Dell M109S) and a digital USB CCD camera (Model: The Imaging Source DMK 21BU04). A 12 mm focal-length mega-pixel lens (Model: Computar M1214-MP) is attached to the camera. The resolution of the camera is 640×480 , with a maximum frame rate of 60 frames/s. The pixel size of the camera sensor is $5.6 \mu\text{m} \times 5.6 \mu\text{m}$. The projector has a resolution of 858×600 with a lens of $F/2.0$ and $f = 16.67 \text{ mm}$. To reduce the effect of background lighting, the system is placed in a controlled lighting environment without any additional ambient light.

A linear translation stage is used to provide the desired linear motion backward and forward for error analysis. In this research, we used the TECHSPEC Metric Long Travel Linear Translation Stage. This stage is 250 mm long with a traveling accuracy of 0.1 mm. A uniform, flat white object is mounted on top of the translation stage and travels with the stage for this study. For all positions of the stage, the focal length setting of the projector was kept constant.

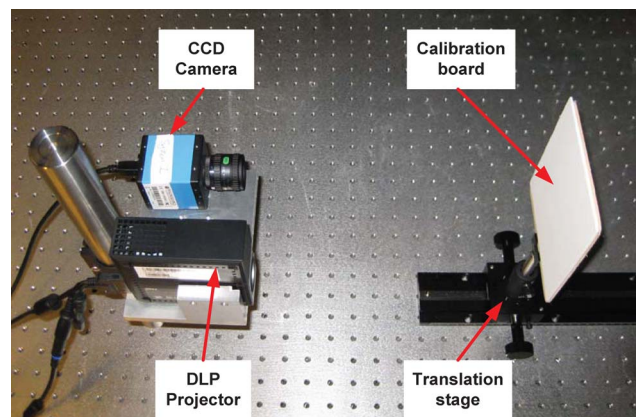


Fig. 4. (Color online) Photograph of the experimental system setup.

B. Phase Error Determination

The algorithm introduced in Subsection 2.D is used to compute the absolute phase value for the binary structured patterns. The phase-shifted fringe patterns are generated by spatially moving the binary structured ones. For instance, a $2\pi/3$ phase shift can be achieved by moving the binary patterns 1/3 of their period. Our experiments found that the absolute phase map, $\Phi^b(x,y)$, of a uniform white board is curved instead of planar. This might be because of camera lens distortion, projector lens distortion, and/or the deviation of the uniform, flat white surface from an ideal plane. This makes it difficult to determine the phase error only from these defocused binary patterns. To circumvent this problem, we also performed the experiments with a conventional fringe generation technique, i.e., the projector projected computer-generated sinusoidal fringe patterns.

We used the multiple-wavelength phase-shifting technique introduced in Subsection 2.C to obtain the absolute phase values for the conventional fringe patterns. Because the commercial DLP projector is typically a nonlinear device, the nonlinearity could introduce periodic phase error in the conventional fringe patterns if it is not handled properly. Numerous approaches have been proposed to either actively [15,16] or passively [17–20] correct the errors caused by nonlinear gamma. In this research, we used a technique introduced in [16] to actively deform the projected fringe patterns. We have demonstrated that, after compensation, the periodic phase error caused by nonlinear gamma is alleviated to a negligible level. Moreover, because the DLP projector uses time modulation to generate grayscale images, the exposure time must be properly controlled [3]. In this research, we used the exposure time of 1/30 s to avoid the problems associated with synchronization. From these fringe patterns, another absolute phase map, $\Phi^s(x,y)$, can be obtained. If the fringe pitch, i.e., the number of pixels per fringe stripe, is the same as that used for the binary patterns, the difference between these two phase maps gives the phase error induced by the binary structured point patterns, that is, the phase error is calculated point by point using

$$\Delta\Phi(x,y) = \Phi^b(x,y) - \Phi^s(x,y). \quad (16)$$

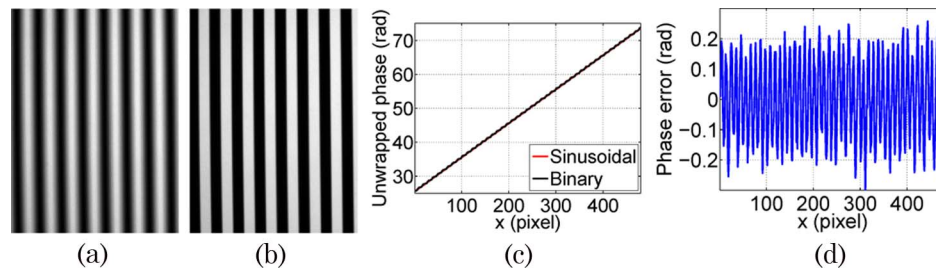


Fig. 5. (Color online) Phase errors computed by finding the difference between the phase obtained from the sinusoidal fringe patterns and that obtained from the defocused binary patterns. (a) One of the three phase-shifted fringe patterns used in the sinusoidal method. (b) One of the three phase-shifted fringe patterns used in the binary method. (c) Cross sections of the absolute phase maps. (d) Phase error.

Here, $\Phi^b(x,y)$ represents the absolute phase from the binary structured patterns, and $\Phi^s(x,y)$ represents the absolute phase from the sinusoidal fringe patterns.

It should be noted that this phase error is the error relative to the conventional fringe projection technique; thus the result obtained from a conventional fringe projection technique is held up as the gold standard for this study. To reduce the influence of the random noise caused by $\Phi^s(x,y)$, this phase map was smoothed by a 9×9 Gaussian filter. Figure 5 shows a typical result obtained by the aforementioned methods. To reduce the measurement error caused by object color, we only used black/white (B/W) fringe patterns for both the conventional and the defocusing methods. The B/W fringe patterns are generated by setting the grayscale values of the red, green, and blue channels of the projector to be equal to each other. Figure 5(a) shows one of the three phase-shifted sinusoidal fringe patterns, and Fig. 5(b) shows one of the defocused binary patterns. It can be seen that there are obvious binary structures in the binary fringe pattern. Figure 5(c) shows the cross sections of the absolute phase maps, $\Phi^s(x,y)$ and $\Phi^b(x,y)$. This figure indicates that they are indeed closely aligned together, and the difference between them will be the phase error, as shown in Fig. 5(d). The error appears to have a periodic structure that could be further analyzed for error compensation. It should be noted that to reduce the subpixel sampling difference between the fringe patterns captured for these two methods, the phase error is shifted to ensure that its average is 0.

The phase error shown in Fig. 5(d) is spatially position dependent and thus is difficult to use for further analysis. To solve this problem, we plot the phase error map against the wrapped phase, $\phi(x,y)$, as shown in Fig. 6(a). In this figure (as well as the remaining figures), one cross section of the absolute phase map is depicted. (We took great care in our experimental procedures to ensure that the patterns deviate negligibly from the vertical. Because of this, each horizontal cross section can be treated as representative of the others.) This clearly shows that the phase error appears to be spatially position independent in the phase domain, which is desirable for future error compensation purposes. Moreover, the error map also has very obvious structures. To

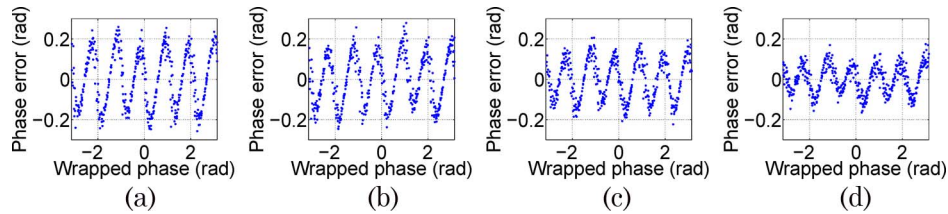


Fig. 6. (Color online) Phase error maps for different depth planes. (a) Depth $z = 0$ mm, (b) depth $z = 40$ mm, (c) depth $z = 80$ mm, and (d) depth $z = 120$ mm.

further verify these, we captured three additional planes and plotted the phase errors against the wrapped phase [as shown in Figs. 6(b)–6(d)]; they all appear to have similar structures as in Fig. 6(a) but different amplitudes. The similarity between the phase errors in different planes provides the opportunity to find a mathematical description of the phase error in terms of the wrapped phase value, $\phi(x, y)$, and the depth value, z . Once the function is determined, it can be used to compensate for the associated phase error. Because it is deterministic, the phase error function can be found from calibration, which will be addressed next.

C. Phase Error Function Estimation: DSP

To calibrate the phase error function in terms of the wrapped phase, $\phi(x, y)$, and the depth, z , we set up the system in a manner so that the projected image is focused onto a plane, and the camera is also focused at the same plane. This plane is chosen as $z = 0$. We then move the plane towards the system with an increment of $\Delta z = 5$ mm. For each plane, we recorded the three phase-shifted and four coded binary patterns for the binary phase map $\Phi^b(x, y)$ and the 15 phase-shifted sinusoidal patterns for the sinusoidal phase map $\Phi^s(x, y)$. Both the binary and the sinusoidal phase-shifted patterns had the same fringe pitch. We computed the phase error using Eq. (16). Because the phase error is depth z dependent and wrapped phase ϕ dependent, we can rewrite the phase error equation as

$$\Delta\Phi(x, y; z) = \Phi^b(x, y; z) - \Phi^s(x, y; z) = f(\phi; z). \quad (17)$$

To simplify the error function determination, we do the following two steps for each plane.

- Step 1: Create an M -element LUT by evenly quantizing the wrapped phase $[-\phi, +\phi]$ for the entire

image, including all cross sections, with a $2\pi/M$ rad phase interval. Within each interval, the phase error is averaged to reduce the random error for the whole image. In this research, we use a 1024-element array to store the error LUT. Figure 7(a) shows the LUT for the whole image of which a portion of a cross section is illustrated in Fig. 6(a). Media 2 shows the series of LUTs arranged in order of increasing depth z value. It clearly indicates that the phase error LUTs also have similar structures but different amplitudes.

- Step 2: Fit the LUT with an N th-order polynomial of the form $\Delta\Phi(x, y; z) = \sum_{k=0}^N \alpha_k(z)\phi^k$. We found that a 40th-order polynomial is necessary in order to precisely represent the error LUT because of its complex structures. Figure 7(b) shows the overlay between the fitted polynomial and the original LUT. They seem to be aligned well with each other.

To verify the effectiveness of an LUT and its associated polynomial fitting, we used them to compensate for the phase errors in their own particular plane. Figure 7(c) shows the residual error after error compensation with the LUT of Fig. 7(a), while Fig. 7(d) shows the residual error after error compensation with its associated fitted polynomial. The phase error is reduced from its original value of RMS 0.137 rad to RMS 0.041 rad with the LUT and to RMS 0.051 rad with the fitted polynomial. It is approximately three times smaller for both methods. The polynomial fitting method performs slightly worse than the direct LUT method, because it has some approximation during the optimization stage. One may notice that after error compensation, not only is the magnitude of the phase error significantly reduced, but also the periodic structure of the phase error is significantly diminished. Because the phase errors after compensation appear to be random, a standard random noise reduction method (e.g., a Gaussian filtering) can be adopted to further reduce their

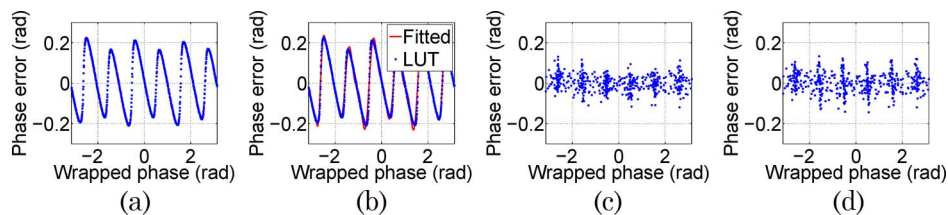


Fig. 7. (Color online) Phase error compensation using an LUT and its associated polynomial fitting. (a) The LUT in terms of wrapped phase value (Media 2). (b) The polynomial-fitted curve. (c) The residual error after compensation using the LUT shown in (a) (RMS: 0.041 rad). (d) The residual error after compensation using the fitted polynomial (RMS: 0.051 rad).

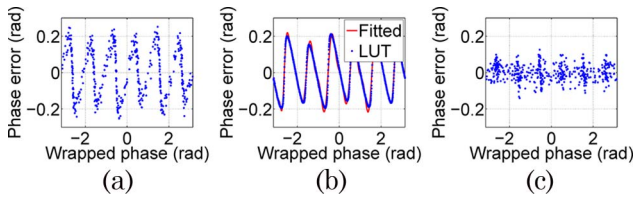


Fig. 8. (Color online) Error compensation using the DSP method. (a) The original error (RMS: 0.129 rad). (b) The original LUT and the polynomial fitting. (c) Phase error after compensation (RMS: 0.045 rad).

influence. This experiment demonstrated the effectiveness of phase error reduction by both the original LUT-based method and the polynomial-based approach.

The error fitting approach introduced above is called the intraplane error fitting. Figure 6 as well as the associated Media 2 show that the phase error is depth z dependent. Once the error functions for different depths are determined, the polynomial coefficients can be further fitted with polynomials in terms of distance z . These polynomials are called the interplane error fitting. Finally, the error function can be written in the following equation:

$$\Delta\Phi(x, y; z) = \sum_{k=0}^N \left(\sum_{l=0}^M c_{k,l} z^l \right) \phi^k. \quad (18)$$

Here, $c_{k,l}$ are constants. In this research, we found that at least an $N = 40$ th-order polynomial is needed for intraplane fitting, and at least $M = 3$ rd-order polynomials are needed for the interplane fitting (coefficient fittings).

To calibrate the phase error function, we measured 26 planes at distance intervals of $\Delta z = 5$ mm. Among these planes, 19 of them were used for the polynomial function calibration, and the remaining planes were used for validation purposes. The phase errors for each of these calibration planes were calculated and fitted with intraplane polynomials, and the coefficients of these polynomials were further fitted with interplane polynomials. Once the coefficients $c_{k,l}$ were determined, the function could be used for error compensation.

D. Phase Error Function Calibration: PLUT

As addressed previously, because the intraplane error function is very complex, it is difficult to approximate it with a low-order polynomial, and we used a 40th-order polynomial to represent this function. Even though this polynomial seems to perform rea-

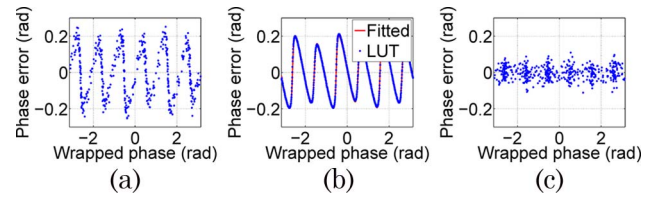


Fig. 9. (Color online) Error compensation using the PLUT method. (a) The original error (RMS: 0.129 rad). (b) The original LUT and the calculated LUT. (c) Phase error after compensation (RMS: 0.037 rad).

sonably well, it results in two problems: (1) the computation cost is high because this operation needs to be performed point by point, which makes the whole process very slow; and (2) because a high-order polynomial is used, the computational error may influence the accuracy of error compensation if the algorithm is not optimized.

We thus proposed a second method; instead of fitting the intraplane error function with a polynomial, the error LUT data are directly utilized. For each element in the LUT that represents a particular wrapped phase range ($2\pi/M$ rad), the interplane polynomial functions are generated through optimization. Because of the similarity between the phase error structures at different depths, we found that only 3rd-order polynomials are needed. Because this method essentially uses an M -element LUT of polynomial functions of z , it is called the PLUT method.

It is important to note that for both methods, we chose polynomials to represent the error function for simplicity. The error can also be represented with other means, such as B -splines, piecewise splines, etc.

4. Experimental Results

To verify the performance of the error functions obtained above, we tried to compensate for the phase error of a plane that was not used for the polynomial function calibration ($z = 20$ mm). Figure 8(a) plots the original error against the wrapped phase. The RMS error is found to be 0.129 rad. To find out the correctness of using DSP to represent the phase error of this plane, we calculated the LUT directly from the phase error measured for this particular plane and compared it to the phase error computed using the calibrated polynomial function in Eq. (18) with a depth value of $z = 20$ mm. Figure 8(b) shows the result. This experiment indicates that the calibrated polynomial function well represents the error function of this plane, and thus it can be used to compensate for the error of this plane. Figure 8(c) shows the

Table 1. Phase Error Before and After Error Compensation with Both Methods for Different Depth z Values

Depth z (mm)	20	40	55	60	80	95	120
Raw (rad)	0.129	0.123	0.115	0.113	0.099	0.090	0.069
DSP (rad)	0.045	0.043	0.040	0.040	0.037	0.037	0.040
PLUT (rad)	0.037	0.037	0.035	0.036	0.032	0.031	0.030

^aThe error shown in this table is the RMS value in radians.

result after compensation. The RMS value is dramatically reduced from 0.129 to 0.045 rad, and the error map appears to be random, similar to the compensated error maps for those planes that were used to estimate the error function. This experiment verified the success of the proposed error compensation approach to compensate for the phase error in an arbitrary plane.

As a comparison, we used the PLUT method to compensate for the phase error of the plane used in Fig. 8. Figure 9 shows the result. It can be seen that PLUT can better represent the original phase error and thus better compensate for the error. After compensation, the phase error is reduced to approximately RMS 0.037 rad, which is similar to the result with the DSP method. However, this error pattern looks more random than the one compensated by the DSP method (which still has some clear structures). Table 1 summarizes the phase error before and after error compensation for both methods, and it clearly indicates that the PLUT method always outperforms the DSP method. It should also be noted that when the fringe pattern becomes nearly sinusoidal, the phase error is already very small, and both methods only slightly reduce the error.

As explained in Subsection 2.E, the depth z can be determined from the absolute phase pixel by pixel using Eq. (15). In this equation, there are only two unknowns, c_0 and z_0 . If these two unknowns are determined, the phase error compensation algorithm can be applied to an arbitrary 3D surface.

To determine these two unknowns in Eq. (15), we use the set of planes captured for error function estimation. For each plane k , we precisely know its absolute depth value z^k and the absolute phase value for one particular camera pixel (e.g., central pixel), Φ_0^k . From these data, the depth $z(\Phi_0)$ as a function of one particular pixel's absolute phase Φ_0 can be determined. Therefore, once that particular pixel's absolute phase is known for the reference plane, its depth z_0 can be determined.

The constant c_0 can also be determined from these data. Because of the approximately linear relationship between the phase difference ($\Delta\Gamma_0^k = \Delta\Phi_0^k - \Delta\Phi_0^{k-1}$) and the depth changes ($\Delta z^k = z^k - z^{k-1}$), we can estimate the constant c_0 by using a least-squares algorithm.

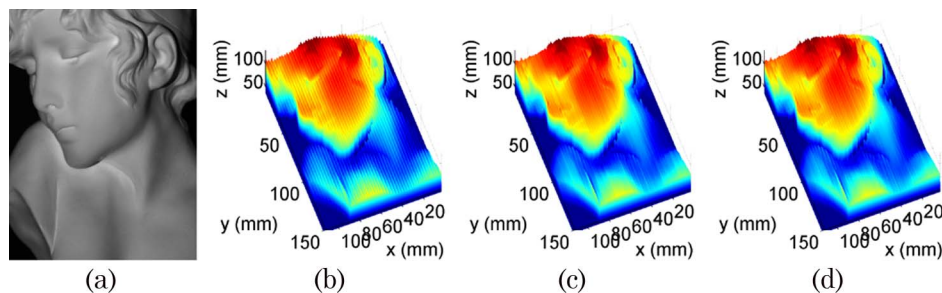


Fig. 11. (Color online) Experimental results for a complex 3D object. (a) Photo of object, (b) 3D result before compensation, (c) 3D result after applying the DSP method, and (d) 3D result after applying the PLUT method.

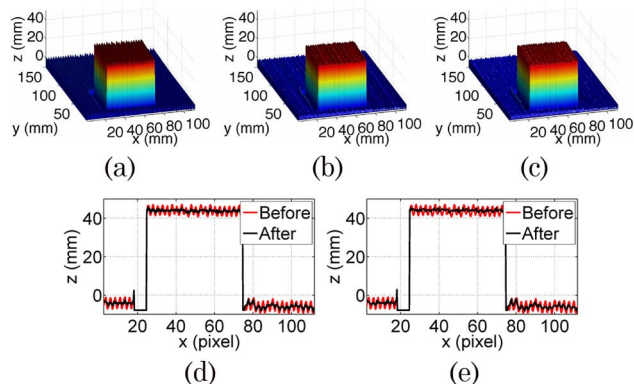


Fig. 10. (Color online) Experimental results for a step-height object. (a) 3D result before compensation, (b) 3D result after applying the DSP method, (c) 3D result after applying the PLUT method, (d) 480th row cross sections of original data and the result after applying the DSP method, and (e) 480th row cross sections of the original data and the result after applying the PLUT method.

Once the depth z is determined for each point, the phase error $\Delta\Phi(x,y)$ can be determined since the wrapped phase $\phi(x,y)$ is already known. Therefore, the phase error can be compensated point by point for an arbitrary 3D shape.

We verified the proposed approach by measuring a simple 3D object: a step-height object with two flat surfaces at different depths. The surface was measured by the binary defocusing method, as shown in Fig. 10(a). It clearly shows large measurement errors (stripes). We then compensated for the phase error using the DSP and the PLUT methods, as shown in Figs. 10(b) and 10(c), respectively. It can be seen that the stripes are less clear in both cases, yet the latter case looks slightly better. To better compare these results, one cross section of each of the results is plotted, as shown in Figs. 10(d) and 10(e). This clearly shows that the proposed approach can be used to compensate for the phase errors of a 3D object.

In addition, a more complex 3D surface was measured to further verify the performance of the proposed approach. Figure 11 shows the measurement result. Again, both proposed error compensation algorithms perform well, with the PLUT method being slightly better.

5. Summary

This paper has presented a method to compensate for the phase error caused by binary structured

patterns. The preliminary experimental results showed that the error function can be approximated as a polynomial function in terms of wrapped phase, $\phi(x, y)$, with coefficients that can be approximated as polynomial functions of depth, z , and that this phase error function can be determined by calibration. Once the error function is calibrated, it can be used to compensate for the phase errors caused by different defocusing levels, which correspond to different depths z . Experiments were conducted and verified that this DSP approach could significantly reduce the phase error and also could effectively alleviate the periodic structure of the original phase errors. However, we used a 40th-order polynomial to represent the intraplane phase error function, which was very time consuming for calculations and had the potential to result in computational inaccuracies. To circumvent this problem, we developed another method called PLUT to compensate for this type of error. Experiments found that it outperforms the DSP method only slightly, yet the computational cost was much lower. Thus, the PLUT method is more suitable for high-speed applications.

References

1. S. Gorthi and P. Rastogi, "Fringe projection techniques: whither we are?," *Opt. Lasers Eng.* **48**, 133–140 (2010).
2. S. Zhang, "Recent progresses on real-time 3-D shape measurement using digital fringe projection techniques," *Opt. Lasers Eng.* **48**, 149–158 (2010).
3. S. Lei and S. Zhang, "Digital sinusoidal fringe generation: defocusing binary patterns VS focusing sinusoidal patterns," *Opt. Lasers Eng.* **48**, 561–569 (2010).
4. S. Lei and S. Zhang, "Flexible 3-D shape measurement using projector defocusing," *Opt. Lett.* **34**, 3080–3082 (2009).
5. L. J. Hornbeck, "Digital light processing for high-brightness, high-resolution applications," *Proc. SPIE* **3013**, 27–40 (1997).
6. Y. Gong and S. Zhang, "High-speed, high-resolution three-dimensional shape measurement using projector defocusing," *Opt. Eng.* **50**, 023603 (2011).
7. Y. Gong and S. Zhang, "Ultrafast 3-D shape measurement with an off-the-shelf DLP projector," *Opt. Express* **18**, 19743–19754 (2010).
8. M. Takeda and K. Mutoh, "Fourier transform profilometry for the automatic measurement of 3-D object shape," *Appl. Opt.* **22**, 3977–3982 (1983).
9. S. Zhang, D. van der Weide, and J. Olivier, "Superfast phase-shifting method for 3-D shape measurement," *Opt. Express* **18**, 9684–9689 (2010).
10. X. Y. Su, W. S. Zhou, G. Von Bally, and D. Vukicevic, "Automated phase-measuring profilometry using defocused projection of a Ronchi grating," *Opt. Commun.* **94**, 561–573 (1992).
11. D. Malacara, ed., *Optical Shop Testing*, 3rd ed. (Wiley, 2007).
12. D. C. Ghiglia and M. D. Pritt, *Two-Dimensional Phase Unwrapping: Theory, Algorithms, and Software* (Wiley, 1998).
13. S. Zhang, "Digital multiple-wavelength phase-shifting algorithm," *Proc. SPIE* **7432**, 74320N (2009).
14. S. Zhang, "Flexible 3-D shape measurement using projector defocusing: Extended measurement range," *Opt. Lett.* **35**, 931–933 (2010).
15. S. Kakunai, T. Sakamoto, and K. Iwata, "Profile measurement taken with liquid-crystal grating," *Appl. Opt.* **38**, 2824–2828 (1999).
16. P. S. Huang, C. Zhang, and F.-P. Chiang, "High-speed 3-D shape measurement based on digital fringe projection," *Opt. Eng.* **42**, 163–168 (2003).
17. S. Zhang and P. S. Huang, "Phase error compensation for a three-dimensional shape measurement system based on the phase shifting method," *Opt. Eng.* **46**, 063601 (2007).
18. S. Zhang and S.-T. Yau, "Generic nonsinusoidal phase error correction for three-dimensional shape measurement using a digital video projector," *Appl. Opt.* **46**, 36–43 (2007).
19. H. Guo, H. He, and M. Chen, "Gamma correction for digital fringe projection profilometry," *Appl. Opt.* **43**, 2906–2914 (2004).
20. B. Pan, Q. Kemao, L. Huang, and A. Asundi, "Phase error analysis and compensation for nonsinusoidal waveforms in phase-shifting digital fringe projection profilometry," *Opt. Lett.* **34**, 416–418 (2009).